A Comparison of the Tribo-Mechanical Properties of a Wear Resistant Cobalt-Based Alloy Produced by Different Manufacturing Processes

H. Yu

R. Ahmed[1]
e-mail: r.ahmed@hw.ac.uk

School of Engineering and Physical Sciences,
Heriot-Watt University,
Edinburgh EH14 4AS, UK

H. de Villiers Lovelock
Deloro Stellite,
Cheney Manor Industrial Estate,
Swindon SN2 2PW, UK

This paper aims to compare the tribo-mechanical properties and structure–property relationships of a wear resistant cobalt-based alloy produced via two different manufacturing routes, namely sand casting and powder consolidation by hot isostatic pressing (HIPing). The alloy had a nominal wt % composition of Co–33Cr–17.5W–2.5C, which is similar to the composition of commercially available Stellite 20 alloy. The high tungsten and carbon contents provide resistance to severe abrasive and sliding wear. However, the coarse carbide structure of the cast alloy also gives rise to brittleness. Hence this research was conducted to comprehend if the carbide refinement and corresponding changes in the microstructure, caused by changing the processing route to HIPing, could provide additional merits in the tribo-mechanical performance of this alloy. The HIPed alloy possessed a much finer microstructure than the cast alloy. Both alloys had similar hardness, but the impact resistance of the HIPed alloy was an order of magnitude higher than the cast counterpart. Despite similar abrasive and sliding wear resistance of both alloys, their main wear mechanisms were different due to their different carbide morphologies. Brittle fracture of the carbides and ploughing of the matrix were the main wear mechanisms for the cast alloy, whereas ploughing and carbide pullout were the dominant wear mechanisms for the HIPed alloy. The HIPed alloy showed significant improvement in contact fatigue performance, indicating its superior impact and fatigue resistance without compromising the hardness and sliding/abrasive wear resistance, which makes it suitable for relatively higher stress applications.
[DOI: 10.1115/1.2736450]

Keywords: Stellite 20, HIPing, abrasive wear, sliding wear, fatigue

1 Introduction

The cobalt-based alloys, which are also known as Stellite[2] alloys, were originally developed by Elwood Haynes in the 1900s and are widely used in wear-related applications, particularly in lubrication-starved, high-temperature, or corrosive environments. The excellent wear resistance of cobalt-based alloys benefits from the martensitic FCC to HCP phase transformation of cobalt, the solid solution strengthening by tungsten/molybdenum, and the formation of hard carbides [1–5]. These cobalt-based alloys are primarily used in the form of castings, powder metallurgy (PM) parts, hot isostatic pressing (HIPing) consolidated parts, weld hard facings (using powder, rod, or wire consumables), laser hard facings, and thermal spray coatings.

The alloy selected for this investigation had a high tungsten and carbon content with a nominal wt % composition similar to the commercially available Stellite 20 alloy (Co–33Cr–17.5W–2.5C). Its relatively high carbon content leads to high volume fraction of carbides in the microstructure, which provides high hardness, strength, and wear resistance. As one of the most abrasion resistant cobalt-based alloys, mainly due to its higher tungsten and carbon contents, this alloy is generally used in applications such as pump sleeves, rotary seal rings, wear pads, and bearing sleeves. Despite high hardness and abrasion/wear resistance of this alloy, the coarse carbide structure in the castings often results in brittleness. The processing and machining of cast cobalt alloys therefore poses a challenge due to phase transformations, and coarse carbide structure, respectively. Carbide refinement is one way to improve the alloy performance, which can be achieved by varying the processing route, e.g., from casting to HIPing. HIPing is a thermo-mechanical material processing technique that can be used for casting densification, powder consolidation, cladding, and diffusion bonding. The HIPing process involves the simultaneous applications of pressure (up to 200 MPa) and temperature (over 2000°C) in a HIPing vessel. For powder consolidation, the powder is generally sealed in a can of steel or similar material, and placed inside the HIPing vessel to simultaneously apply temperature and isostatic pressure with an inert gas such as argon or nitrogen. The heating and cooling rates are carefully controlled. The HIPing time, temperature, and pressure are selected on the basis of powder particle size and material for full densification. Metallurgical bonding between the powder particles starts with necking at the interface of powder particle boundaries. The mechanisms of diffusion, bonding, and porosity closure during the HIPing process have been a topic of research of a number of investigations. HIPing of cobalt-based alloys can therefore provide additional benefits in terms of finer microstructure, near net shape parts consolidated to full density, and improved mechanical properties, which can provide an attractive combination of prop-

[1]Corresponding author.

[2]Stellite is a registered trade name of Deloro Stellite Company Inc.

Contributed by the Tribology Division of ASME for publication in the Journal of Tribology. Manuscript received March 15, 2006; final manuscript received January 9, 2007. Review conducted by Thierry Blanchet. Paper presented at the STLE/ASME 2006 International Joint Tribology Conference (IJTC2006), San Antonio, TX, USA, October 22–25, 2006.

Table 1 The chemical compositions of cast and HIPed alloys (wt %)

	Co	Cr	W	C	Mo	Fe	Ni	Mn	Si
Cast alloy	Bal.	34.50	16.50	2.39	0.50	1.50	1.00	0.60	0.78
HIPed alloy	Bal.	31.85	16.30	2.35	0.27	2.50	2.28	0.26	1.00

erties for the design process. However, the investigations related to the structure–property relationship of these alloys produced via different processing routes (especially HIPing) are limited in the published literature. Hence this paper aims to provide comparative investigations of the tribo-mechanical properties on the basis of structure–property relationship of Stellite 20 alloys, produced via two different processing routes of sand casting and powder consolidated HIPing. These investigations were made on the basis of the microstructural comparisons via scanning electron microscopy (SEM), energy dispersive x-ray spectroscopy (EDS), and x-ray diffractometry (XRD). Tribo-mechanical evaluations involved hardness, impact toughness, abrasive wear, sliding wear, and contact fatigue performance tests.

2 Experimental Test Procedure

2.1 Materials and Microstructure. The HIPed alloy was produced via canning the gas-atomized powders at 1200°C and 100 MPa pressure for 4 h. The sieve analysis (+250 μm: 0.1 wt %, −250 μm+180 μm: 1.5 wt %, −180 μm+125 μm: 6.4 wt %, −125 μm+45 μm: 61.9 wt %, −45 μm: 29.7 wt %) of powders indicated that most of the powders were less than 125 μm, and generally of spherical morphology due to the atomization process. The cast alloy samples were produced via sand casting. Table 1 summarizes the chemical compositions of both the cast and HIPed alloys. The microstructure of the powders and both alloys was observed via SEM using a backscattered electron imaging (BEI) detector. The chemical compositions of different phases developed in the powders and alloys were determined via EDS and XRD with Cu K_α radiation ($\lambda = 1.5406$ Å). Image analysis was also conducted to ascertain the volume fractions of individual phases.

2.2 Hardness and Un-notched Charpy Impact Tests. The Vickers hardness was measured at both macro- and microlevels. A conventional Avery hardness tester was used to measure the macrohardness under a load of 294 N. Five measurements were conducted on each alloy. The microhardness was measured using a MVK-H1 hardness tester under a load of 2.94 N. Thirty measurements were conducted on each sample. The un-notched Charpy impact tests were carried out on the samples with dimensions of 10 mm × 10 mm × 55 mm, using an Avery impact tester at an impact rate of 5 m/s. Three tests were conducted on each alloy.

2.3 Abrasive Wear Tests. The abrasive wear performance of both alloys was investigated via the dry sand rubber wheel (DSRW) abrasion tests (ASTM G65 standard (Procedure B)) [6]. During the testing, the alloy sample, with dimensions of 6 mm × 25 mm × 75 mm, was forced under a load of 130 N against the rubber wheel, which rotated at a speed of 200 rpm ± 5 rpm. The outer polyurethane rim of the wheel had a diameter of 228.6 mm and a hardness of Shore A-60. Two types of silica sand particles were used as abrasives in the current work. Both were dry and rounded, but they were different in their size distribution. Sand A had a larger average particle size, with at least 85 wt % particles having sizes between 150 μm and 300 μm. For Sand B, 85 wt % particles had sizes within the range of 90–180 μm. The silica sand was introduced between the sample and the rubber wheel, with sand flow rate of about 330 g/min. Each test lasted a total of 2000 revolutions, which was controlled by a revolution counter. Three tests were conducted on each material with Sands A and B, respectively. The wear mass loss of the sample was weighed to the nearest 0.001 g. The abrasive wear test results were reported as volume loss, which was computed from the mass loss and the density of the alloy.

2.4 Sliding Wear Tests. The sliding wear performance of the alloys was investigated via the reciprocating ball-on-flat test method. These tests were conducted on a bench mounted wear test machine using a tungsten carbide ball (93.5–94.5% WC, and 5.5–6.5% Co) and a cobalt alloy disk sample under a normal load of 25 N. The ball radius was 6.35 mm. The disk sample had a diameter of 31 mm and thickness of 8 mm. During the test, the disk sample experienced reciprocating sliding motion at an oscillating frequency of 1.0 Hz with a stroke length of 10 mm. The total sliding distance was 500 m for each test. The friction force was measured via a tension–compression load cell. Three tests were conducted on each alloy. The wear volume loss of the disk sample was computed from the stroke length and the average cross-sectional area of the wear groove, which was measured via an interferometer.

2.5 Rolling Contact Fatigue Tests. The rolling contact fatigue (RCF) tests were conducted on a modified four-ball machine, as illustrated in Fig. 1, details of which can be appreciated from Stewart et al. [7]. Three Si_3N_4 ceramic balls with diameter of 4.76 mm were equispaced at 120 deg using a polymer spacer, and driven by a 31-mm-diameter cobalt alloy disk sample. The rotary speed of the drive shaft was set at 5000 rpm, and the total contact load was varied as 120 N and 180 N. The lubricant used in the RCF tests was Exxon Turbo 2389. The λ value was approximated between 1.4 and 1.8, indicating that the tests were carried out under a mixed elasto-hydrodynamic lubrication (EHL) regime. The RCF failure was detected by the increase in the vibration amplitude of the cup assembly above a preset level.

3 Experimental Results

3.1 Microstructure and Phase Analysis. Figure 2(*a*) shows the fine dendritic microstructure on the cross section of gas-atomized powder used for HIPing. Figure 2(*b*) shows the hypereutectic microstructure of cast alloy. It consists of rod-like primary Cr-rich carbides (dark phase showing section of rod-like primary carbide), lamellar W-rich carbides (light phase), and the

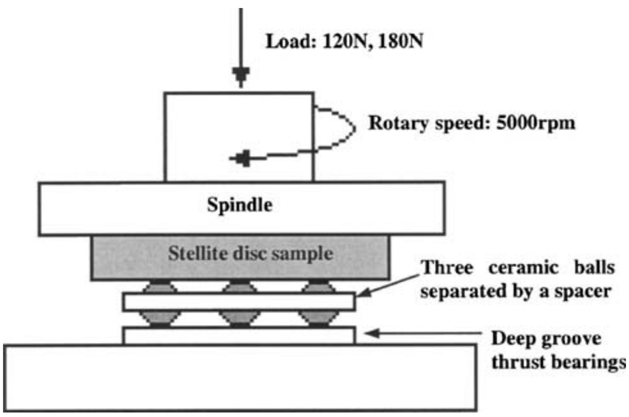

Fig. 1 Schematic illustration of the cup assembly for the rolling contact fatigue tests

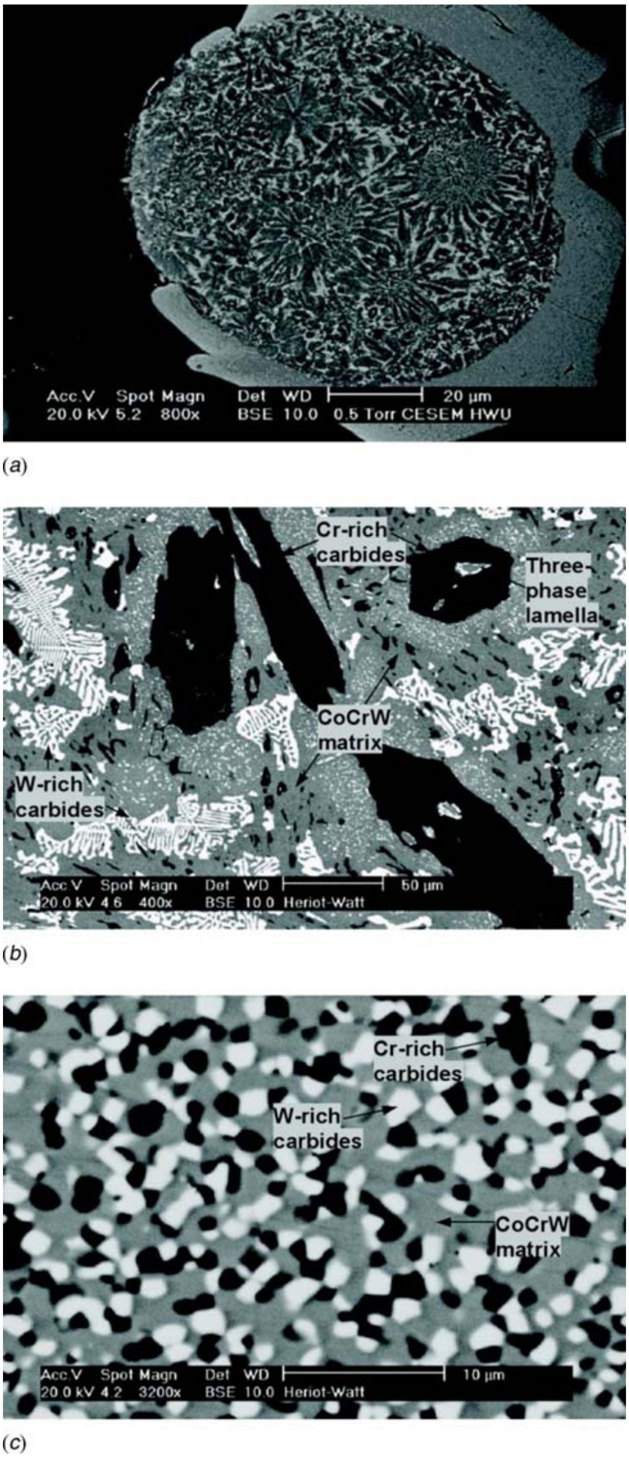

Fig. 2 The SEM images showing the microstructure of: (*a*) powder cross section; (*b*) cast alloy; and (*c*) HIPed alloy

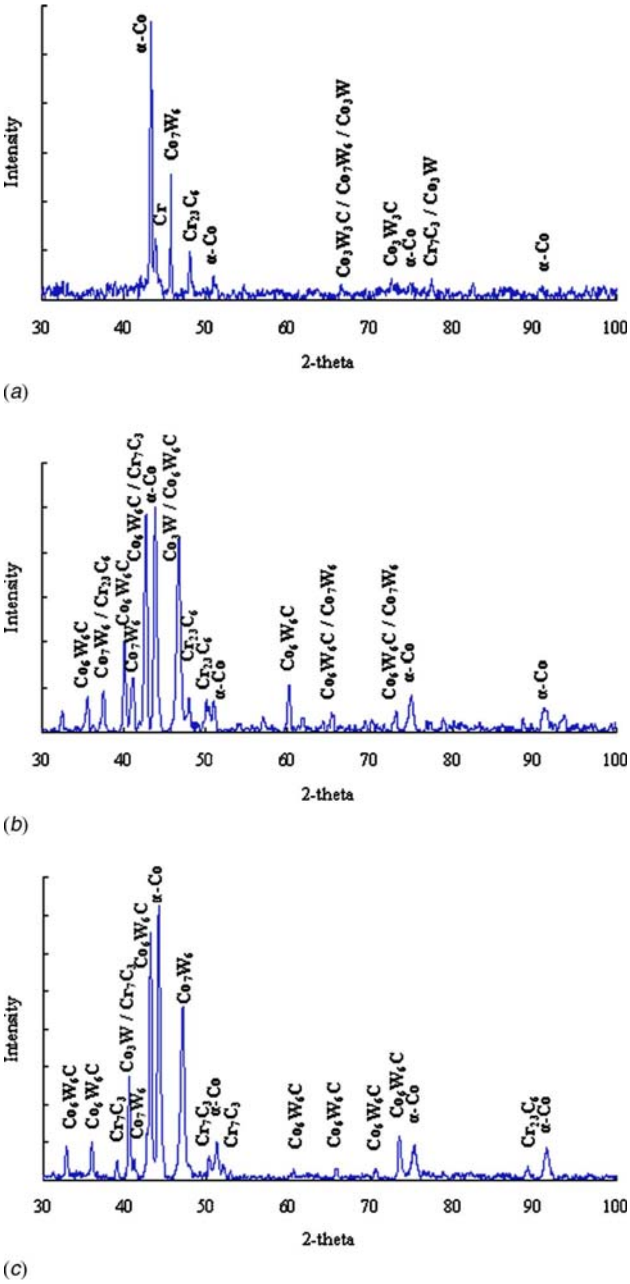

Fig. 3 XRD patterns of: (*a*) alloy powder; (*b*) cast alloy; and (*c*) HIPed alloy

CoCrW matrix (grey region). The microstructure of HIPed alloy is shown in Fig. 2(*c*), in which the fine carbides (Cr-rich dark phase and W-rich light phase) are uniformly distributed in the matrix (grey region). Figure 3 summarizes the XRD patterns of atomized powder, cast, and HIPed alloys. The possible phases are also given on the basis of the crystallographic database. Table 2 lists the image analysis results.

3.2 Hardness and Charpy Impact Tests. The macro-, micro-hardness, and un-notched Charpy impact energy results of both alloys are summarized in Table 3. Both alloys had similar average macrohardness, although the cast alloy had higher average micro-hardness. The HIPed alloy showed impact energy which was ap-

Table 2 The volume fractions of individual phases in cast and HIPed alloys

	Cr-rich carbides (dark phase) (%)	W-rich carbides (bright phase) (%)	Co-rich matrix (grey region) (%)
Cast alloy	24.5±2.0	18.1±0.2	57.4±1.8
HIPed alloy	24.2±1.0	24.7±0.7	51.1±1.4

Table 3 The hardness and un-notched Charpy impact energy of cast and HIPed alloys

	Macrohardness (HV, 294 N)	Microhardness (HV, 2.94 N)	Charpy impact energy (J)
Cast alloy	653.4±18.7	759±98	1.36±0.00
HIPed alloy	675.0±17.2	704±15	9.26±2.18

proximately an order of magnitude higher than the cast counterpart. The fractographs of failed areas are shown in Fig. 4.

3.3 Abrasive Wear Tests. Figure 5 presents the average volume loss of both alloys after the DSRW tests. The cast alloy showed better abrasive wear resistance than the HIPed alloy in the tests with Sand A. Both alloys had higher wear loss when finer sand (Sand B) was used, however the cast alloy was affected more by the size effect of sand particles, which resulted in similar wear loss of both alloys with Sand B. The wear scars after the DSRW tests are shown in Fig. 6.

3.4 Sliding Wear Tests. Figure 7 presents the average volume loss of the disk samples after the ball-on-flat sliding wear tests. Although it was difficult to take precise measurement of ball material loss, the observations on the ball surface indicated that some material was removed on the surface of tungsten carbide balls wearing against the cast alloy disks, while the balls wearing against the HIPed alloy disks were almost unworn, as illustrated schematically in Fig. 8. Therefore the total wear loss of test couples, for both alloys against the tungsten carbide ball, was similar although the average wear loss of the HIPed alloy was more than that of the cast samples. Figure 9 shows typical SEM observations of the wear scars after the sliding wear tests.

3.5 Rolling Contact Fatigue Tests. The results of stress cycles to failure in the RCF tests are summarized in Fig. 10. These results indicate that for both stress levels of 3.1 GPa and 3.6 GPa, fatigue resistance of the HIPed alloy was at least two orders of magnitude superior than its cast counterpart. The HIPed alloy test at 3.1 GPa was suspended after 75.6×10^6 stress cycles without failure. Figure 11 shows the failure observations of both alloys. Cast alloy failed by spalling at an approximate depth of

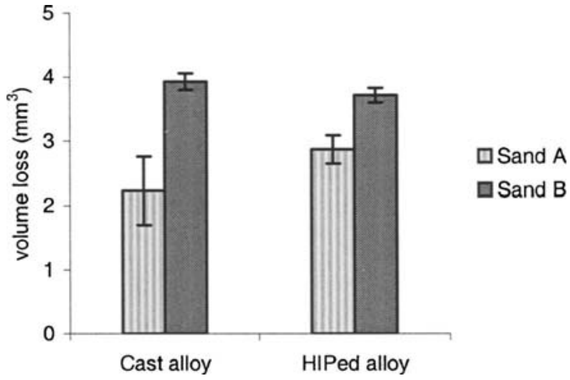

Fig. 5 Average volume loss of cast and HIPed alloys after the dry sand rubber wheel tests

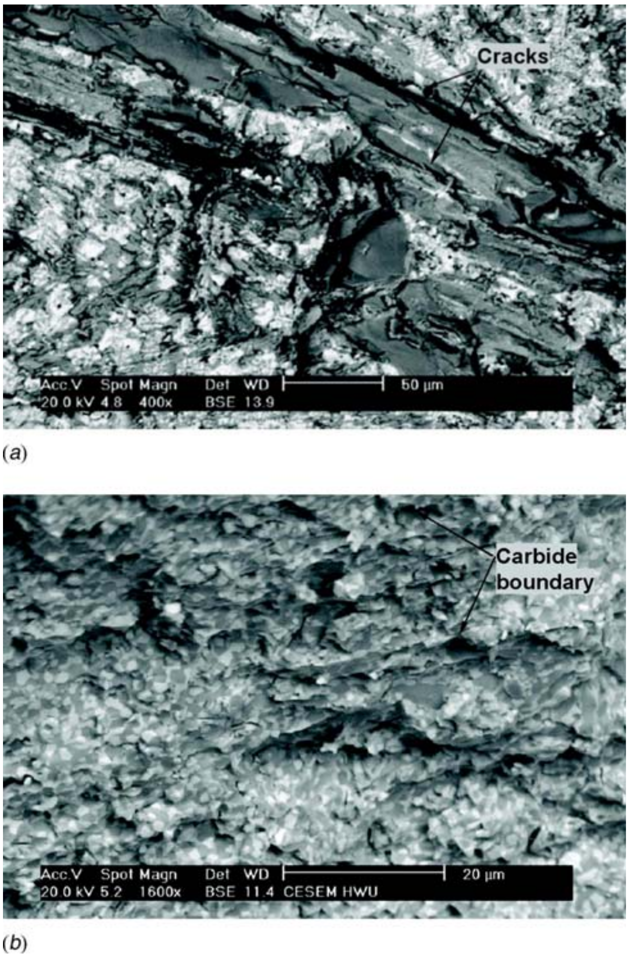

Fig. 4 The fractographs after the un-notched impact test on: (*a*) cast alloy; and (*b*) HIPed alloy

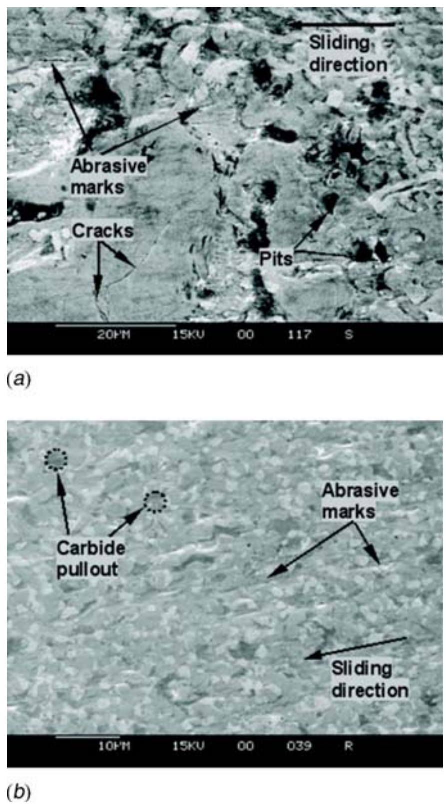

Fig. 6 The wear scars after the dry sand rubber wheel tests with sand B on: (*a*) cast alloy; and (*b*) HIPed alloy

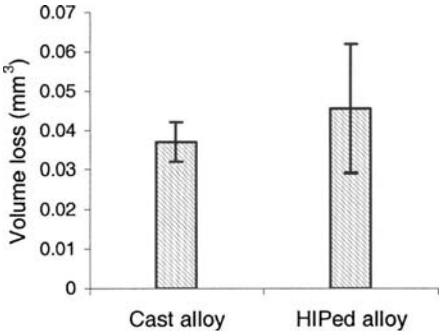

Fig. 7 Average disk volume loss of cast and HIPed alloys after the ball-on-flat wear tests

28–41 μm, whereas the failure in the HIPed alloy was surface distress at a relatively shallower depth of 7–28 μm. Table 4 provides a summary of the contact conditions during the fatigue tests.

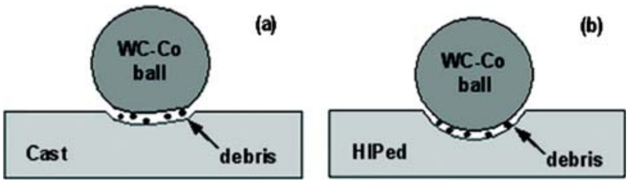

Fig. 8 Schematic representation showing the ball-on-flat sliding wear tests between: (*a*) cast disk and WC–Co ball (some wear on the ball); and (*b*) HIPed disk and WC–Co ball (no appreciable wear on the ball surface)

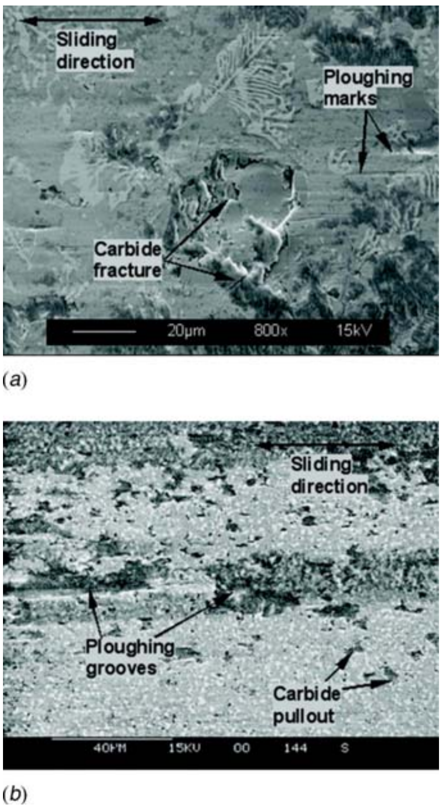

Fig. 9 The wear scars after the ball-on-flat tests of (*a*) cast alloy; and (*b*) HIPed alloy

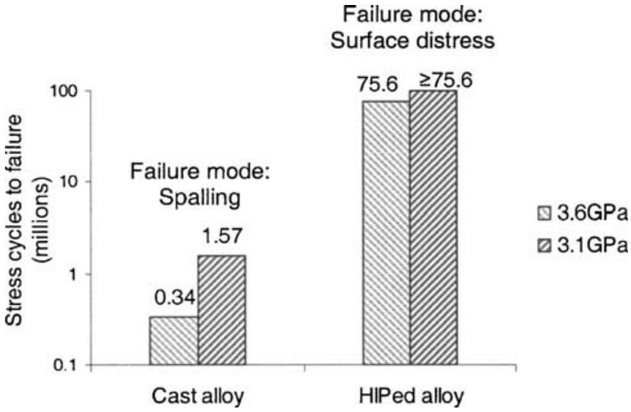

Fig. 10 The stress cycles to failure of cast and HIPed alloys after the rolling contact fatigue tests

The depths of the orthogonal shear stress, $Z_{\text{orth(max)}}$, and maximum shear stress, $Z_{\tau(\max)}$ in Table 4 are given by the following equations [8]

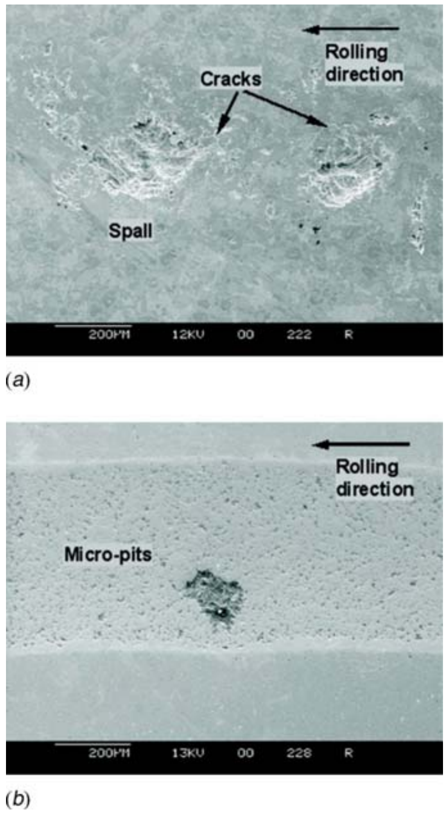

Fig. 11 The wear tracks after the contact fatigue tests on: (*a*) cast alloy, 3.6 GPa; and (*b*) HIPed alloy, 3.6 GPa

Table 4 Contact parameters during the rolling contact fatigue (RCF) tests of cast and HIPed alloys

Contact stress P_0 (GPa)—Eq. (4)	3.1	3.6
Total load (N)	120	180
Contact width $2a$ (μm)—Eq. (3)	156	198
Orthogonal shear stress depth (μm)—Eq. (1)	27	35
Maximum shear stress depth (μm)—Eq. (2)	37	48

$$Z_{\mathrm{orth(max)}} \cong 0.35a \quad (1)$$

$$Z_{\tau(\mathrm{max})} \cong 0.48a \quad (2)$$

where a is the radius of the contact area, which is given by the Hertzian point contact equation [9]

$$a = \left(\frac{3wr}{4E^*}\right)^{1/3} \quad (3)$$

in which w is the normal load; r is the radius of the ceramic ball; and E^* is the combined Young's modulus which depends on the Young's modulus and the Poisson's ratio of the contacting materials. The maximum contact stress, P_0, is given by the following equation

$$P_0 = \frac{3w}{2\pi a^2} \quad (4)$$

4 Discussion

4.1 Microstructure. The microstructure of cobalt-based (Stellite) alloys has been the topic of research for almost a century and a number of investigations have discussed their microstructure on the basis of alloy composition and processing route [4,5,10–17]. However, comparative analysis of the microstructure of these alloys is scarce in the published literature. The aim of the discussion here is therefore to highlight the differences in the microstructure of the two alloys, with a view to underpin the understanding of structure–property and tribo-mechanical behavior.

The cast alloy had a hypereutectic microstructure, which was typical of cobalt-based alloys of this composition. The primary idiomorphic carbide was Cr-rich M_7C_3, with a composition of $(Cr_{0.75}Co_{0.20}W_{0.05})_7C_3$, as approximated by the EDS analysis. These are rod like carbides, a section of which can be seen as the dark blocky carbide in Fig. 2(*b*). It was surrounded by the dendritic CoCrW solid solution (grey region). The final phases to solidify were the lamellar eutectic phases containing both the Cr-rich (dark) and W-rich (light) carbides. The three-phase area shown in Fig. 2(*b*) indicates the simultaneous occurrence of both primary carbides and CoCrW dendrites in the microstructure. The XRD analysis (Fig. 3(*b*)) revealed that the carbides were Cr_7C_3, $Cr_{23}C_6$, and Co_6W_6C, while the primary phase in the solid solution was α-cobalt (fcc), together with the intermetallic compounds, Co_3W and Co_7W_6. Hence, in the cast alloy, there were three kinds of carbides, i.e., the relatively large blocky Cr-rich carbides, the interconnected three-dimensional W-rich eutectic carbides, and the relatively smaller Cr-rich eutectic carbides, which coexisted in the microstructure.

The HIPed alloy had a finer microstructure (Fig. 2(*c*)) with Cr-rich (dark) and W-rich (light) carbides uniformly distributed in the matrix. These carbides were typically 2 μm in size and much finer than the large blocky carbides observed in the cast alloy. Despite different microstructure, the possible phases identified in the HIPed alloy were similar to those in the cast alloy (Fig. 3). These phases seemed to be inherited from the atomized powders, except for the replacement of Co_3W_3C by Co_6W_6C. The pure chromium phase identified in the powder, which formed due to the rapid solidification from the molten state during the atomization process, was not identified in the HIPed alloy. This indicated that it either was combined with cobalt, or formed carbides, and no longer existed as a pure phase after the HIPing process.

The total volume fraction of carbides (Table 2) was nearly 50% in the HIPed alloy, which were uniformly distributed in the metal matrix (Fig. 2(*c*)). The differences in the carbide morphology of both alloys can have a significant influence on their tribo-mechanical properties. In terms of the structure–property relationships, as discussed in later sections, the failure mechanisms, which were very much dependent upon crack propagation, e.g., impact and fatigue strength, therefore benefitted significantly from the absence of a three-dimensional eutectic net in the HIPed alloy. However, there was a tradeoff between the improved impact strength and relatively lower wear resistance due to smaller carbides in the HIPed alloy, because of the changes in the wear mechanisms during the abrasive and sliding wear of the two alloys. The image analysis (Table 2) indicated that despite similar volume fractions of Cr-rich carbides in both alloys, the approximate W-rich carbides content in the HIPed alloy (24.7%) was more than that in the cast alloy (18.1%). In view of the higher carbide content, one might expect superior abrasive and sliding wear performance of the HIPed alloy. However, as discussed later, the changes in the wear mechanisms due to the relatively smaller size of carbides observed in the HIPed microstructure, did not provide significant abrasive wear improvement over the cast counterpart.

4.2 Hardness and Impact Energy. It is widely accepted that the contents of carbon and tungsten play a dominant role in the hardness of cobalt-based alloys. Both the formation of hard carbides and solid solution strengthening by tungsten can enhance hardness [4,13,18,19]. In the current investigation, the presence of M_7C_3, $Cr_{23}C_6$, and Co_6W_6C carbides in both alloys was beneficial to their hardness. The intermetallic compounds, i.e., Co_3W and Co_7W_6, also strengthened the solid solution and increased the matrix hardness. The HIPed alloy had slightly higher macrohardness than the cast alloy, which was mainly due to its slightly higher carbide fraction (Table 2). The indentation diagonal length in the macrohardness measurements was typically 0.28 mm, which was much bigger than the typical carbide size for both alloys (30–150 μm for the cast alloy, 2 μm for the HIPed alloy), or the spacing between the carbides (matrix phase), and hence provided a reliable measure of the hardness of both alloys with low standard deviation. At the microlevel, however, both the cast and HIPed alloys showed higher average hardness than those measured at the macroscale. Additionally, the average microhardness of the cast alloy was significantly higher than the HIPed counterpart. Three factors are thought responsible for this behavior, i.e., (1) relationship between carbide size and indentation size; (2) higher standard deviation of the microhardness of cast alloy; and (3) observations of carbide cracks after the indentation of cast alloy. The indentation diagonal length during the Vickers microhardness test was around 26–28 μm, which was smaller than the size of the blocky carbides in the cast alloy, but an order of magnitude bigger than the carbide size in the HIPed alloy. Hence microhardness measurements were very sensitive to the location of indentation in the cast alloy. In some cases, the indentation was located well within the carbide and in others between the carbide and matrix. Hence there was a relatively larger variation of microhardness values in the cast alloy, as seen in the standard deviation value. In some cases large blocky carbides of the cast alloy also fractured under the indentation load, which also influenced the hardness values when compared to the HIPed alloy, where there was no evidence of carbide fracture.

The Charpy impact energy absorption represents the impact toughness of the alloy under dynamic conditions. During the impact tests, brittle fracture took place along and within the coarse carbides in the cast alloy, followed by rapid crack propagation, as indicated by a number of macrocracks observed in Fig. 4(*a*). The fractograph indicated that the blocky Cr-rich M_7C_3 carbides were the main propagation path for cracks, due to their large size and brittle character. Contrary to this, the HIPed alloy showed intergranular fracture, where cracks initiated and propagated along the carbide/matrix and carbide/carbide boundaries (Fig. 4(*b*)). The fracture within the carbide particles of the HIPed alloy was not appreciable. As these carbides were relatively fine, the fracture path had to change direction frequently along the carbide/matrix and in some cases carbide/carbide boundaries before transforming into macrocracks. The finer microstructure along with the matrix ductility therefore provided the crack arrest mechanism. Contrary to this, although the matrix in the cast alloy had similar composition and hence expected to provide similar assistance for the crack arrest mechanisms, the preferred crack propagation route was not at the carbide/matrix boundary, or through the matrix, but within the large blocky carbides and the eutectic net. Once microcracks initiated, they readily propagated to form macrocracks within the coarse blocky carbides, avoiding the matrix.

4.3 Abrasive Wear Performance. Previous investigations have indicated that the abrasive wear resistance of cobalt-based alloys is influenced not only by the hardness of the alloy [12], but also by the volume content, size, and morphology of the carbides [3,12,13,20]. The coarse carbides seen in the cast alloy seemed to be of great benefit to the abrasive wear resistance. The possible abrasive wear mechanisms include microfracture of the carbides [21], micromachining of the matrix [14], and carbide pullout [14,22].

The cast alloy showed superior abrasive wear resistance to the HIPed alloy in the tests with the coarse Sand A, whereas both alloys showed similar resistance in the tests with relatively finer Sand B. This is attributed to the size distribution of sand particles in relation to the size of coarse carbides in the cast alloy, i.e., the size of Sand A was generally larger than the blocky carbide size (30–150 μm), whereas Sand B was similar in size to most of the large blocky carbides, which comprised almost 25% of the microstructure. The dominant wear mechanisms during these tests were different, which were identified via the investigation of the worn surfaces. The abrasive wear of cast alloy involved brittle fracture of the blocky carbides and ploughing of the matrix. Figure 6(*a*) indicates the cracks on the carbides and the ploughing tracks in the matrix region. The angularities of the abrasive sand particles could result in a high normal load (or stress) on the large blocky carbides and/or the three-dimensional eutectic region in the cast alloy. If the normal load exceeded a critical value, w^*, the cracks would form [9]

$$w^* \propto \left(\frac{K_{IC}}{H}\right)^3 K_{IC} \tag{5}$$

where K_{IC} is the fracture toughness and H is the hardness. However, the brittle fracture on the coarse carbides in the cast alloy did not account for a large amount of material removal, because the carbides were interlocked in the matrix even after they fractured, as discussed later. The coarse microstructure of the cast alloy also offered relatively large spaces among the hard carbides, where silica sand with small size could enter and plough. The sharp angularities of the sand particles resulted in preferential microcutting of the matrix. Pits were also observed on the surface of the cast alloy, indicating preferential pullout of smaller lamellar carbides (Figs. 2(*b*) and 6(*a*)). It is appreciated that this mechanism accelerated with finer sand (B) for the cast alloy, and was responsible for the relatively lower abrasive wear resistance of the cast alloy when compared to the coarse Sand A (Fig. 5).

For the HIPed alloy, brittle fracture of the carbides was not widespread. Ploughing of the matrix and the pullout of the carbides were the main wear mechanisms. The abrasive marks observed in Fig. 6(*b*) indicate that the carbides were simply pulled out during the abrasive wear process. Detailed examination of the wear scars also indicated that the abrasive grooves were generally smaller than the average carbide size in the HIPed alloy, and the carbides were seen protruding from the matrix. These observations indicated preferential wear of the matrix, prior to the carbide pullout. This mechanism was similar to those previously reported, where carbide pullout and pit formation were the dominant wear mechanisms in the fine carbide alloys [14], and also cermet coatings of similar carbide size [23]. As both sands used in the investigation were much larger in size than the typical carbide size (2 μm) in the HIPed alloy, the changes in sand particle size resulted in less variation in abrasion resistance than the cast alloy (Fig. 5).

The carbide morphology therefore significantly influenced the dominant abrasive wear mechanisms, i.e., brittle fracture in the cast and carbide pullout in the HIPed alloy. Due to the fine microstructure of the HIPed alloy, the contact load applied on each carbide grain was relatively low, as the load applied by individual sand particles was shared between a number of carbides and the matrix. Therefore the normal load on a single carbide grain was unlikely to reach the critical value for brittle fracture, w^* (Eq. (5)). This can be understood from a simple back of the envelope calculation of the contact area (Eq. (3)) formed at the interface of abrasive (sand) particles and alloy. As the sand particles were rounded, for an approximate calculation they can be modeled as spheres of 150 μm diameter ($2r$, which was typical of the sand size used in this investigation). Although it is almost impossible to know the exact number of sand particles, and the load shared by each of them within the contact region of the DRSW tests at a given time, a conservative approach can be adapted to assume that the loading (w) on a given sand particle, responsible for carbide cracking, can be on the order of 1% (1.3 N) of the total normal load (130 N) during the DSRW test. This is not unlikely given the fact that for an absolute minimum (idealized) loading of each sand particle, the load should be uniformly distributed by a single layer of sand particles (as multiple layers will mean less particles directly in contact with the alloy due to random distribution), within the apparent contact area (or wear scar area of typical dimensions 1.5 cm × 1 cm). This provides a maximum number of sand particles as 6000 in a single layer for minimum loading, and they can coexist between the rubber wheel and alloy interface at any time. If each sand particle then carries equal load (i.e., minimum loading condition), it will be on the order of 0.02 N. However, not all sand particles enter the contact region, and are not loaded equally or perfectly circular in shape, hence the assumption of 1% load can be justified as the first approximation. Based upon this model, the contact diameter ($2a$) calculated from Hertzian calculations (Eq. (3)) of elastic loading can be approximated as ≥20 μm. This area[3] will grow further with the increase in sand particle diameter, increase in loading of individual particles, plasticity effects, frictional effects, and roll/slide ratio. Contact area of this dimension, based upon a conservative model, therefore indicates that the contact diameter is an order of magnitude bigger than the carbide size (approximately 2 μm) in the HIPed alloy. Hence individual carbide particles are only subjected to a small fraction of total load on a given sand particle. This reduces the tendency of carbides to crack in the HIPed alloy, as critical load w^* (Eq. (5)) is less likely to be reached. This was confirmed by the SEM observations of the wear tracks, where only a negligible proportion of carbides fractured in the HIPed alloy.

Contrary to this, individual large blocky carbides in the cast alloy had to sustain much higher contact load, as the entire contact area ($2a \geq 20$ μm) could be located on a single carbide particle (30–150 μm). There was therefore a much higher probability that the loading resulting from such contact conditions on an individual carbide particle could exceed the critical value w^*, and result in its brittle fracture. The value of contact stress approximated from Eq. (4) for this simplified model, can be estimated to give a typical contact stress of approximately 5 GPa, which is high enough to fracture a carbide. However, despite significant fracture of carbides in the cast alloy, their abrasive wear performance was similar to or better than the HIPed alloy (Fig. 5). This was because despite being fractured, some fragments of carbide remained interlocked within the main body of the carbide, due to complex crack propagation within the blocky three-dimensional carbide. This prevented these fragments of cracked carbides from being pulled out, and hence did not contribute to the volume loss

[3]Even if the loading is approximated as 0.1% (0.13 N), the contact diameter ($2a$) will be ≥9 μm.

measured after the DSRW tests (Fig. 5). In the HIPed alloy, once the matrix was abraded by the abrasive sand particles, the carbides were left vulnerable. The fine carbides in HIPed alloy were not able to withstand ploughing due to their two-dimensional structure, as opposed to the large blocky and three-dimensional eutectic net in the cast counterpart. Hence carbide pullout was the dominant wear mechanism in the HIPed alloy.

Other factors such as spacing between carbides, especially in relation to the sand particle size and shape, can also influence abrasive wear performance. Hence, the difference between the performance of the cast and HIPed alloys might differ if even finer sand particles are used. This is because the finer abrasive particles could plough the matrix between the carbides more easily, and result in more material removal. Hence, even finer sand particles than those considered in this investigation may further elaborate the differences in the wear mechanisms of the cast and HIPed alloys. Additional factors, although not considered in this investigation, can be the difference between the carbide/matrix interfacial bond strength of the cast and HIPed alloys.

4.4 Sliding Wear Performance. In the sliding wear tests against the WC–Co ball, the cast disk sample showed slightly better wear resistance than the HIPed alloy. The carbides in the WC–Co ball were much smaller (typically 2 μm, manufacturers data) than the carbides in the cast alloy, resulting in appreciable wear of the WC–Co ball (Fig. 8(*a*)). However, the carbides in the HIPed alloy were similar in size to those in the WC–Co ball, which resulted in negligible wear of the WC–Co ball (Fig. 8(*b*)). Therefore the ball volume loss was significantly higher for the cast alloy, which should ultimately reduce the difference in the total sliding wear volume loss of the test couples for the two alloys. However, as the ball wear scar in the cast alloy couple was nonuniform, its volume loss could not be evaluated using the three-dimensional interferometer.

Previously published results on the sliding wear performance of Stellite alloys indicated that the wear mechanisms consisted of the fracture of the hard carbides [24], the oxide layer [15,25,26], and the predominant wearing of the matrix [16]. Some indicated that under severe sliding wear the influence of microstructure on the wear loss was limited [5]. In this investigation, better wear resistance of the cast alloy is attributed to its coarse microstructure. As the harder counterface, the WC–Co ball could plough through the alloy, and the relatively softer matrix was worn preferentially. The surfaces became rugged due to the remaining protruding carbides. After cyclic loading by the WC–Co ball, cracks initiated on the blocky carbides. Figure 9(*a*) shows the cracks on the carbides in the cast alloy, indicating brittle fracture occurred there. However these carbides in the cast alloy were coarse and interlocked in the matrix. Even after the fracture, they could still be retained in the microstructure due to the interlaced net in the cast alloy. Therefore, the carbides in the cast alloy resisted pullout and ploughing, and therefore reduced the wear loss significantly. For the HIPed alloy, ploughing and carbide pullout were the main wear mechanisms. The groove shown in the middle of Fig. 9(*b*) was wide enough to plough away a number of carbides together with the matrix in a single groove. The pits on the worn surface indicated carbide pullout was widespread in the HIPed alloy.

4.5 Contact Fatigue

.

4.5.1 RCF Performance. The improvement in the impact toughness of the HIPed alloy also resulted in significant improvement in its relative fatigue performance (Fig. 10). This improvement in performance was observed at two different loads of 120 N and 180 N (Table 4), and was indicative of a consistent trend in performance improvement. These results confirm that in addition to the well known abrasive and sliding wear resistance of these alloys, the HIPing processing route provides additional benefits for the use of these alloys in high-impact and fatigue resistance application. This processing route therefore provides a unique blend of tribo-mechanical properties, e.g., hardness, toughness, abrasive/sliding/impact, and fatigue wear, which was not observed in the cast counterpart.

4.5.2 RCF Failure Modes. The contact fatigue failure modes in polycrystalline materials vary from catastrophic delamination and macropitting/spalling to micropitting and surface distress [8,27–33]. The failure mechanisms underpinning these failure modes are based upon the theories of surface and subsurface stress risers. For the case of cermets and other ductile materials, subsurface stress risers, e.g., the orthogonal shear stress (Eq. (1)) and maximum shear stress (Eq. (2)), generally result in crack initiation and propagation [31–33] for fatigue failure. For the case of ceramics and other materials with negligible ductility, maximum tensile stress at the edge of the contact region initiates and propagates fatigue cracks. The SEM investigations of the wear tracks (Fig. 11(*a*)) indicated that the cast alloy failed via spalling, and at a depth which was representative of the maximum shear stress. Spalling failure mode was observed on the worn surfaces of cast alloy tested under both stress levels (3.1 GPa and 3.6 GPa), and microcracks were also visible at the edge of the spalls (Fig. 11(*a*)). The failure mode for the HIPed counterpart was surface distress, which is generally defined as microscale spalling fatigue, at a slightly shallower depth of orthogonal shear stress. A number of micropits were observed in the wear track of HIPed alloy, and it was evident that during the fatigue test, some of the micropits transformed to macropits (Fig. 11(*b*)). Further details of these fatigue failure mechanisms can be seen elsewhere [8]. The widths of the wear tracks (400–500 μm) observed under the SEM were greater than the computed contact widths in Table 4, which is attributed to the plastic deformation and/or wear on the sample surfaces during the fatigue testing, and the influence of material shakedown effects during the first few cycles of testing [27,28].

In terms of the structure–property relationships, similar mechanisms of crack propagation were influential as were discussed for the Charpy impact and abrasive wear tests (Secs. 4.2 and 4.3). Once subsurface cracks initiated at the depths of orthogonal or maximum shear stresses, they readily transformed into macrocracks under cyclic loading along the eutectic net and/or within the blocky carbide of the cast alloy. Contrary to this, propagation of subsurface fatigue cracks at these depths in the HIPed alloy was resisted due to the absence of blocky carbides, which provided a relatively easy crack propagation route in the cast alloy. Hence for the HIPed alloy, the subsurface cracks had to propagate through the metal matrix and at the carbide/matrix boundary, which provided resistance to crack propagation during the RCF failure.

5 Conclusion

The main conclusions can be summarized as follows:

(1) The cast alloy had a hypereutectic microstructure, while the HIPed alloy had a much finer microstructure with fine carbides uniformly distributed in the matrix. Microstructural phases in both alloys, however, were similar, i.e., α-cobalt, M_7C_3, $Cr_{23}C_6$, Co_3W, Co_7W_6, and Co_6W_6C;

(2) Despite similar hardness of the two alloys, the impact toughness of the HIPed alloy was approximately an order of magnitude higher than that of cast alloy. This improvement in the impact resistance was attributed to the fine carbide morphology of the HIPed alloy, which resisted crack propagation;

(3) Smaller sand particle size could result in more abrasive volume loss for both the cast and HIPed alloys. Brittle fracture of the carbides and ploughing of the matrix were the main wear mechanisms for the cast alloy, whereas for the HIPed alloy, ploughing and carbide pullout were the dominant wear mechanisms; and

(4) The relative contact fatigue performance of the HIPed alloy

was more than two orders of magnitude better than the cast alloy. This was attributed to the higher impact toughness and finer carbide morphology of the HIPed alloy, which resisted fatigue crack propagation. The main failure mode was spalling for the cast and surface distress for the HIPed alloy.

References

[1] Crook, P., 1991, "Cobalt and Cobalt Alloys," *ASM Handbook*, Vol. 2, ASM, Materials Park, OH, pp. 446–454.

[2] Crook, P., 1994, "Cobalt-Base Alloys Resist Wear, Corrosion, and Heat," Adv. Mater. Processes, **145**(4), pp. 27–30.

[3] Antony, K. C., 1983, "Wear-Resistant Cobalt-Based Alloys," J. Met., **35**(2), pp. 52–60.

[4] De Brouwer, J. L., and Coutsouradis, D., 1966, "Influence of Tungsten and Carbon Contents on the Microstructure and Properties of a Cobalt-Base Hardfacing Alloy," Cobalt (Engl. Ed.), **32**, pp. 141–147.

[5] Frenk, A., and Kurz, W., 1994, "Microstructural Effects on the Sliding Wear Resistance of a Cobalt-Based Alloy," Wear, **174**, pp. 81–91.

[6] ASTM, 2000, *ASTM G65-00 Standard Test Method for Measuring Abrasion Using the Dry Sand/Rubber Wheel Apparatus*, ASTM International, West Conshohocken, PA.

[7] Stewart, S., Ahmed, R., and Itsukaichi, T., 2004, "Contact Fatigue Failure Evaluation of Post-treated WC-NiCrBSi Functionally Graded Thermal Sprayed Coatings," Wear, **257**, pp. 962–983.

[8] Ahmed, R., 2002, "Rolling Contact Fatigue," *ASM Handbook*, W. T. Becker and R. J. Shipley, eds., Vol. 11, ASM, Materials Park, OH, pp. 941–956.

[9] Hutchings, I. M., 1992, *Tribology: Friction and Wear of Engineering Alloys*, Edward Arnold, London, UK.

[10] Kumar, P., 1986, "Properties in P/M Stellite Alloy No. 6," Prog. Powder Metall., **41**, pp. 415–437.

[11] Berns, H., and Wendl, F., 1985, "Microstructure and Properties of CoCr29W (Stellite 6) in the As-Cast, Forged and Powder Metallurgical Condition," *Proceedings of 2nd International Conference on Cobalt*, Venice, Italy, October, pp. 292–305.

[12] De Mol van Otterloo, J. L., and De Hosson, J. Th. M., 1997, "Microstructure and Abrasive Wear of Cobalt-Based Laser Coatings," Scr. Mater., **36**, pp. 239–245.

[13] Silence, W. L., 1978, "Effect of Structure on Wear Resistance of Co-, Fe-, and Ni-Base Alloys," J. Lubr. Technol., **100**, pp. 428–435.

[14] Desai, V. M., Rao, C. M., Kosel, T. H., and Fiore, N. F., 1984, "Effect of Carbide Size on the Abrasion of Cobalt-Base Powder Metallurgy Alloys," Wear, **94**, pp. 89–101.

[15] So, H., Chen, C. T., and Chen, Y. A., 1996, "Wear Behaviors of Laser-Clad Stellite Alloy 6," Wear, **192**, pp. 78–84.

[16] De Mol van Otterloo, J. L., and De Hosson, J. Th. M., 1997, "Microstructural Features and Mechanical Properties of a Cobalt-Based Laser Coating," Acta Mater., **45**, pp. 1225–1236.

[17] Ashworth, M. A., Bryar, J. C., Jacobs, M. H., and Davies, S., 1999, "Microstructure and Property Relationships in Hipped Stellite Powders," Powder Metall., **42**(3), pp. 243–249.

[18] Ayagaki, M., Ohishi, T., Izumi, S., and Tanaka, T., 1996, "Development of Superior Resistant Alloys by HIP Process and Their Applications," Nippon Steel, Nippon Japan, Nippon Steel Technical Report No. 68, pp. 35–43.

[19] Dawson, R. J., and Foley, E. M., 1990, "P/M Cobalt-Base Wear-Resistant Alloys," *ASM Handbook*, Vol. 1, ASM, Materials Park, OH, pp. 977–980.

[20] Crook, P., and Levy, A. V., 1992, "Friction and Wear of Cobalt-Base Wrought Alloys," *ASM Handbook*, Vol. 18, ASM, Materials Park, OH, pp. 766–771.

[21] Kosel, T. H., Li, S. Z., and Rao, C. M., 1985, "The Size Effect in Abrasion of Dual-Phase Alloys," ASLE Trans., **28**(3), pp. 343–350.

[22] Kim, H. J., and Kim, Y. J., 1999, "Wear and Corrosion Resistance of PTA Weld Surfaced Ni and Co Based Alloy Layers," Surf. Eng., **15**(6), pp. 495–501.

[23] Stoica, V., Ahmed, R., Itsukaichi, T., and Tobe, S., 2004, "Sliding Wear Evaluation of Hot Isostatically Pressed (HIPed) Thermal Spray Cermet Coatings," Wear, **257**, pp. 1103–1124.

[24] Song, J. H., and Kim, H. J., 1997, "Sliding Wear Performance of Cobalt-based Alloys in Molten-Al-added Zinc Bath," Wear, **210**, pp. 291–298.

[25] Wang, L., and Li, D. Y., 2003, "Effects of Yttrium on Microstructure, Mechanical Properties and High-Temperature Wear Behavior of Cast Stellite 6 Alloy," Wear, **255**, pp. 535–544.

[26] Aoh, J. N., and Chen, J. C., 2001, "On the Wear Characteristics of Cobalt-based Hardfacing Layer after Thermal Fatigue and Oxidation," Wear, **250**, pp. 611–620.

[27] Kapoor, A., and Williams, J. A., 1996, "Shakedown Limits in Rolling-Sliding Point Contacts on an Anisotropic Half-Space," Wear, **191**, pp. 256–260.

[28] Wong, S. K., Kapoor, A., and Williams, J. A., 1997, "Shakedown Limits on Coated Surfaces," Thin Solid Films, **292**, pp. 156–163.

[29] Tallian, T. E., 1967, "On Competing Failure Modes in Rolling Contact," ASLE Trans., **10**, pp. 418–439.

[30] Littmann, W. E., 1969, "The Mechanism of Contact Fatigue," *An Interdisciplinary Approach to the Lubrication of Concentrated Contacts*, NASA, Washington, D.C., pp. 309–377.

[31] Engineering Science Data Unit, 1984, *ESDU 78035 Contact Phenomena. I: Stresses, Deflections and Contact Dimensions for Normally Loaded Unlubricated Elastic Components*, IHS ESDU International, London, UK.

[32] Engineering Science Data Unit, 1984, *ESDU 84017 Contact Phenomena. II: Stress Fields and Failure Criteria in Concentrated Elastic Contacts under Combined Normal and Tangential Loading*, IHS ESDU International, London, UK.

[33] Ahmed, R., and Hadfield, M., 2002, "Mechanisms of Fatigue Failure in Thermal Spray Coatings," J. Therm. Spray Technol., **11**(3), pp. 333–349.